Acta Materialia 317 (2026) 122527

Contents lists available at ScienceDirect

Acta Materialia

journal homepage: www.elsevier.com/locate/actamat

Time-resolved evolution of micro-, crystal structure, and temperature field during resonant laser sintering of SnO_2 nanoparticles

Jeldrik Schulte *, Markus Winterer, Martin A. Schroer

Nanoparticle Process Technology, Faculty of Engineering and Cenide, University of Duisburg-Essen, Lotharstr. 1, 47057 Duisburg, Germany

ARTICLE INFO

Keywords:
Resonant laser sintering
Simultaneous SAXS / WAXS
Microstructural evolution
High-speed thermography
SnO_2 nanoparticles
Synchrotron radiation
Grain growth kinetics
Lattice expansion

ABSTRACT

The structural evolution of tin dioxide (SnO_2) nanoparticle films during resonant laser sintering is investigated using simultaneous, time-resolved small-angle (SAXS) and wide-angle (WAXS) X-ray scattering combined with high-speed near-infrared (NIR) thermography. A focused synchrotron X-ray beam enables spatially and temporally resolved probing of structural changes at both the microstructural and crystal structure scale. The evolution of the temperature field is monitored to correlate the structural dynamics with the temperature–time profile and to analyze the grain growth kinetics. The structural changes observed *in situ* are complemented by *ex situ* scanning electron microscopy (SEM) of the evolved microstructure. In addition, the lattice expansion by laser induced heating is determined, and the corresponding thermal expansion coefficients are derived. These space- and time-resolved measurements provide detailed insights into the mechanisms governing resonant laser sintering of SnO_2 nanoparticles.

1. Introduction

Microstructural evolution during processing fundamentally determines the functional properties of materials, in addition to their intrinsic material characteristics [1–3]. Sintering alters the microstructure substantially by complex mass transport modifying particle morphology, grain size, porosity, and defect structure [4]. The resulting microstructure is thus determined by the interplay between diffusion kinetics, grain boundary migration, capillarity-driven densification, and possible phase transformations. Consequently, the temperature-time profile during sintering allows tailoring the materials characteristic based on the processing–structure–property relationship [5–7].

This correlation is particularly critical for nanoparticulate systems, where size-dependent thermodynamic and kinetic effects strongly influence sintering behavior. In such systems, rapid grain growth may eliminate nanoscale features that are essential for functional performance [8–10]. A mechanistic understanding of the governing transport processes is therefore required to control microstructural evolvement during thermal treatment.

Resonant laser sintering provides a versatile processing route for particulate materials, enabling the direct fabrication of dense ceramics with tailored geometries. The process is characterized by localized energy deposition and extreme heating and cooling rates with rather low total laser power [11]. When the laser photon energy is selected above the materials bandgap energy, resonant absorption leads to a heating by electron-phonon interaction [11,12], resulting in steep thermal gradients and thus short characteristic diffusion times. Such conditions, combined with the advanced temporal, spatial, and energy input control capabilities of modern laser systems, enable highly flexible temperature–time profiles, including profiles comparable to ultrafast high-temperature sintering (UHS) [13] regimes. Moreover, non-equilibrium states may be accessed and quenched [14–16], promoting the formation of metastable crystal phases. Besides, reactive laser sintering, a specific form of resonant laser sintering, allows the synthesis of complex oxide phases that are difficult to achieve by conventional sintering routes [17]. The use of nanoparticles enables the exploitation of the size-dependent melting point depression, resulting also in significantly lower sintering temperatures compared to conventional microscale powders. Consequently, the required laser power can be reduced for sintering, facilitating the processing on temperature-sensitive substrates [18,19].

The strong spatial localization of energy input implies that local heterogeneities within the green body can significantly affect the thermal evolution and therefore densification kinetics, grain and particle growth, leading to a highly dynamic process. A quantitative description of the coupling between transient temperature fields and

* Corresponding author.
E-mail address: jeldrik.schulte@uni-due.de (J. Schulte).

https://doi.org/10.1016/j.actamat.2026.122527
Received 1 April 2026; Received in revised form 19 June 2026; Accepted 4 July 2026
Available online 4 July 2026

microstructural dynamics is therefore essential for tailoring the desired structural characteristics. *In situ* X-ray scattering experiments are well suited for this purpose [20–27].

However, resolving structural evolution during laser sintering at relevant time scales and with the required lateral resolution remains experimentally challenging. Simultaneous small- and wide-angle X-ray scattering (SAXS / WAXS) measurements using focused synchrotron radiation are employed to address this challenge, enabling real-time monitoring of crystallite growth, lattice expansion, micro strain, and particle size evolution. The transient temperature field of the laser-irradiated region is independently measured by near-infrared (NIR) high-speed thermography [28] to correlate these structural dynamics with the thermodynamic driving force, enabling the direct comparison between observed structural evolution, and the imposed thermal cycle. This provides the basis for an improved mechanistic understanding and quantitatively validated simulations.

The model system investigated in this study consists of nano-crystalline Tin (IV) oxide (SnO_2) films. SnO_2 exhibits a wide bandgap of ~ 3.57 eV [29] and strong X-ray scattering contrast, making it well suited for resonant UV laser processing and for time-resolved scattering experiments. In addition to the wide field of applications of SnO_2 [30], its optoelectrical performance can be significantly modified by sintering-induced microstructural changes [31].

In the present study, we quantify the micro- and crystal structure evolution during resonant laser sintering by resolving lattice expansion, grain growth kinetics, and particle growth in real time. The experimentally determined temperature–time profiles are directly correlated with structural observables to elucidate the processing–structure relationship during laser treatment. *Ex situ* scanning electron microscopy (SEM) complements the *in situ* measurements and provides further information on the resulting microstructure and morphology.

2. Experimental methods

The *in situ* measurements during resonant laser sintering are carried out at the P62 SAXSMAT beamline at the German Electron-Synchrotron (DESY) [32]. The UV laser and its associated optical components [Fig. 1] are installed at the beamline's experimental site to perform the measurements *in situ* and *operando*.

2.1. Laser sintering set-up

A Helium-Cadmium UV laser (IK 3102 R-G, Kimmon Koha) is used for sintering. The continuous wave (cw) HeCd laser has a wavelength of 325 nm and an output power of 100 mW. The laser beam is directed onto the sample using a set of 4 plane mirrors (041–0325, Eksma Optics) [Fig. S. 1]. Two mirrors are mounted in motorized holders to enable a precise positioning within the micrometer range. The laser beam is focused onto the sample by a $f = 40$ mm focus lens (LA4130-UV, Thorlabs) which is placed in an optical cage system on a *x-y-z* fine positioning stage. The lens is additionally placed on a piezoelectric linear-translation stage (PD1, Thorlabs), to enable a fine adjusting of the focus plane onto the sample surface without changing the position of the focus spot. Pulses of the cw laser beam are generated by an electronic single blade shutter (SH05, Thorlabs) combined with the shutter controller (SC10, Thorlabs), enabling laser pulses as short as 10 ms. The laser power is adjusted by a motorized neutral density filter wheel (NDC-100C-2 M, Thorlabs), which offers an optical density up to 2 OD. The laser power and the transmission after each optical component is measured by a high-sensitivity thermal sensor (3A, Ophir). All motors are remote-controlled enabling the positioning of the laser beam from the control room of the beamline when the X-ray radiation is released.

2.2. Sample preparation

The used SnO_2 nanoparticles are generated by chemical vapor synthesis (CVS). A detailed description of the process can be found in [33, 34]. The primary crystallite size of the pristine powder is determined from X-ray diffraction (XRD) as 8 nm [Fig. S. 2]. The particles are dispersed in ethanol (20 mg / 0.4 ml) using an ultrasonic tip (UP200S, Hielscher). Afterwards 40 µl of dispersion are dropcasted on polyimide foils with a thickness of 125 µm. The resulting SnO_2 film has a thickness in the size range of 1 µm and the film diameter is around 1.5 cm.

2.3. Simultaneous wide- and small angle X-ray scattering

At the beamline, simultaneous wide-angle (WAXS) and small-angle X-ray scattering (SAXS) measurements are performed *in situ* during resonant laser sintering. A focused X-ray beam (40 µm × 25 µm) with a photon energy of 12 keV is used. WAXS patterns are recorded with an Eiger 2 × 4 M area detector in air, while SAXS patterns are collected simultaneously using an Eiger 2 × 9 M in vacuum detector. The detector–sample distance for WAXS is calibrated using a silicon reference sample and is 19.65 cm, corresponding to a detectable q-range of 11 nm^{-1} – 48 nm^{-1}. For SAXS, the detector–sample distance is calibrated with a silver behenate standard to 7.65 m, providing an accessible q-range of 0.04–2.05 nm^{-1}. The 2D scattering patterns are azimuthally integrated using the beamlines data reduction pipeline based on PyFAI [35], yielding in one dimensional scattering profiles $I(q)$. Background measurements are performed at several positions on an uncoated polyimide substrate using the same exposure time as for the sample measurements. A total of 100 frames are recorded, averaged, and subtracted as background signal to improve statistics [Fig. S. 3]. Additionally, several measurements of uncoated polyimide foils are performed [Fig. S. 4 - Fig. S. 5] during and after laser irradiation to ensure that no artefacts arise due to altering of the polyimide.

2.3.1. Alignment procedure

The following alignment strategy is developed to precisely align the laser focus with the position where the X-ray beam passes through the

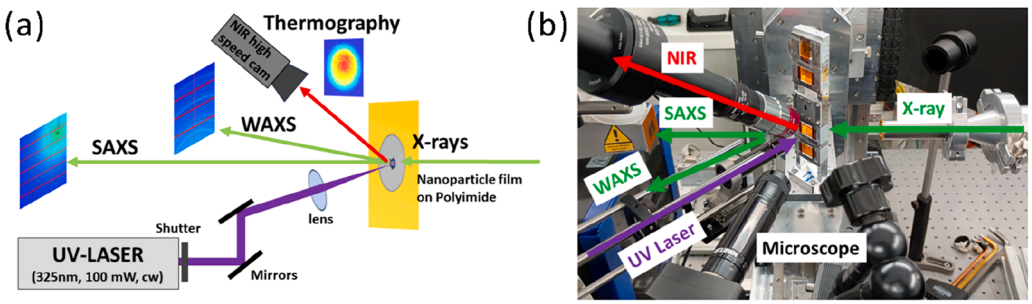

Fig. 1. (a) Schematic drawing of the experimental setup for the *in situ* measurements. The setup enables simultaneous measurements of SAXS and WAXS, combined with NIR high-speed thermography during resonant laser sintering. Only the essential optical components are shown for simplicity. (b) The technical realization of the measurement in the experimental site at beamline P62.

sample: A molybdenum pinhole with a diameter of 100 μm is used to find the position of the focused X-ray beam. The pinhole is moved by a motorized X-Y-Z stage to that position, where the X-ray beam passes the pinhole, as seen by the intensity of the transmitting beam detected by a diode on the beam stop. At this position, the laser beam is adjusted and focused on the pinhole using a microscopic camera, which is sensitive in the UV range. Afterwards, the pinhole is replaced by the sample with the motorized stage, to have the laser sintering spot at the exact same position of the X-ray beam passing through the sample.

2.4. Near-infrared (NIR) high-speed thermal imaging

The NIR high-speed thermal images are recorded with a monochrome chronos 1.4 high-speed camera. The camera is combined with a long pass colorfilter (cut-on 850 nm) and a NIR optimized microscopic optic, whereas the internal infrared filter is removed. The camera is calibrated by heating a SnO_2 film on a silicon substrate [Fig. S. 6 – Fig. S. 8], which is identically prepared as the SnO_2 film used for laser sintering. Details about the NIR high-speed temperature measurements and calibration procedure are explained in [28]. The camera system is positioned at a zenith angle of 45° with respect to the sample surface [Fig. S. 1] and focused using the pinhole [Fig. S. 9] employed for the spatial alignment of the laser and X-ray beams. The optical filter was temporarily removed to increase the detected signal intensity and thereby facilitate accurate focusing. Images are acquired at the full sensor resolution (1280 × 1024 pixels), corresponding to a field of view of 2.425 mm × 1.372 mm at the zenith angle of 45°. Subsequent analysis is performed on a selected region of interest (ROI) extracted from the recorded images.

2.5. Synchronisation

The timing is controlled by a microcontroller (Uno R4, Arduino) operating at a clock speed of 48 MHz. The X-ray detectors provide a TTL signal when acquisition of the first frame begins. This signal is read by the microcontroller at a sampling rate of 10 kHz. After predefined delays, the microcontroller generates TTL-signals to both the laser shutter controller and the NIR high-speed camera, thereby synchronizing the SAXS / WAXS data acquisition, the laser pulse, and the NIR thermal imaging. An exemplary timing profile at a 200 ms laser pulse and a total measurement duration of 1 s is shown in [Fig. S. 10]. For precise timing, the latency between the electric signal for the laser beam shutter and the opening of the shutter is measured with a photodiode (SFH 208, Osram) and a microcontroller (Uno R4, Arduino) with a sampling rate of 25 kHz [Fig. S. 10 (a)]. The measurement indicates a latency of 9 ms and additionally about 500 μs for the mechanical shutter blade to release the laser beam fully (from zero to full intensity).

2.6. Scanning electron microscopy (SEM)

After laser sintering, the sintered spots are characterized *ex situ* by SEM (JSM-7500F, Jeol). Prior to examination, the samples are coated with an 8 nm carbon layer to minimize charging effects.

3. Results and discussion

Time-resolved and combined WAXS and SAXS measurements are performed *in situ* during resonant laser sintering to investigate the kinetics and underlying mechanisms by analyzing the microstructural changes induced by laser irradiation. In addition, the temperature evolution is recorded by high-speed NIR thermal imaging to correlate the temperature-time profile with the evolution of the microstructure.

For this purpose, laser pulses with different pulse length (20 ms up 200 ms) are applied on nanoparticulate SnO_2 films prepared on Kapton (polyimide)-substrates. The Kapton-sheets allow for X-ray measurements in transmission geometry. This geometry is more favorable than a reflection geometry for WAXS as the effective beam size on the sample can be kept smaller (smaller footprint), thus achieving higher spatial resolution. During operation, it became apparent that it is easier to position the sample at an incidence angle of 45° to the X-ray beam [Fig. 1. b] and orthogonal to the laser beam, which facilitates precise focusing on the sample surface. Using a laser pulse with a pulse length of 200 ms, the temperature field evolution and the evolution of the particle and crystal structure is examined in detail. Four experiments with different pulse length (20 ms, 50 ms, 100 ms und 200 ms) are compared, the kinetics of grain growth are evaluated and the thermal expansion of the SnO_2 particles is determined.

3.1. Evolution of the temperature field

Fig. 2 depicts the evolution of the surface temperature during a 200 ms laser pulse. Thermal images are recorded at a frame rate of 500 frames per second (fps) with an exposure time of 1.994 ms. The time t refers to the elapsed time after opening of the laser shutter. The images are stretched by a factor of $\sqrt{2}$ along the vertical axis, to correct for the geometric compression caused by the camera's inclination angle (see Fig. 1(b)). For clarity, only selected frames from the middle of the pulse are shown.

Immediately after the shutter opens, a rapid temperature increase is observed within the first 12 ms. This is followed by a quasi-steady period in which both the temperature level and its spatial distribution remain comparatively constant, although minor temporal evolution and lateral heat propagation are visible. After the laser shutter closes at about 200 ms, the sample cools rapidly, declining below 873 K within approximately 4 ms.

Fig. 3(a) elucidates the temporal evolution of the hot-spot temperature, calculated as the mean of a 3 × 3 pixel area around the pixel with the highest intensity. Following a steep initial rise during the first frames after shutter opening, a maximum temperature of approximately 1200 K is reached. A slight drop in temperature is observed in the middle of the laser pulse. Once the shutter is closed, the temperature falls below 873 K within two frames.

The rapid cooling indicates that only a limited amount of thermal energy is stored in the material during local laser heating, enabling fast thermal relaxation. This may also explain the small temperature decrease observed in the middle of the pulse. Since the temperature responds almost instantaneously to changes in the heat balance, even minor variations in thermal conductivity or heat dissipation within the sample result in measurable temperature changes.

Fig. 3(b) presents the average temperature field of the sintering spot during the timespan in which the temperature is quite isothermal. It is calculated from the frames after the steep increase (frame 10 after shutter opening) up to one frame prior to shutter closure. In this figure, the spatial extent of the laser-heated region is clearly visible. The diameter of the area with temperatures exceeding 1100 K is greater than 50 μm. Thus, the hot-spot exceeds the dimensions of the focused X-ray beam (25 μm × 40 μm). However, a temperature gradient remains within this region, which may contribute to spatial variations in the evolving microstructure.

3.2. Structural evolution at the level of micro- and crystal structure

Fig. 4(a) shows the temporal development of the WAXS diffractograms during a 200 ms laser pulse with a laser power of 65 mW. The diffraction patterns are recorded with a framerate of 100 fps and an exposure time of 9.99 ms for each frame. All diffraction patterns confirm that the nanoparticles consist exclusively of SnO_2 in the rutile phase. No phase transformation is observed during laser sintering, consistent with the high thermodynamic stability of the rutile structure.

The resonant absorption of the laser beam energy leads to a fast heating, evidenced by a systematic shift of the Bragg reflections towards

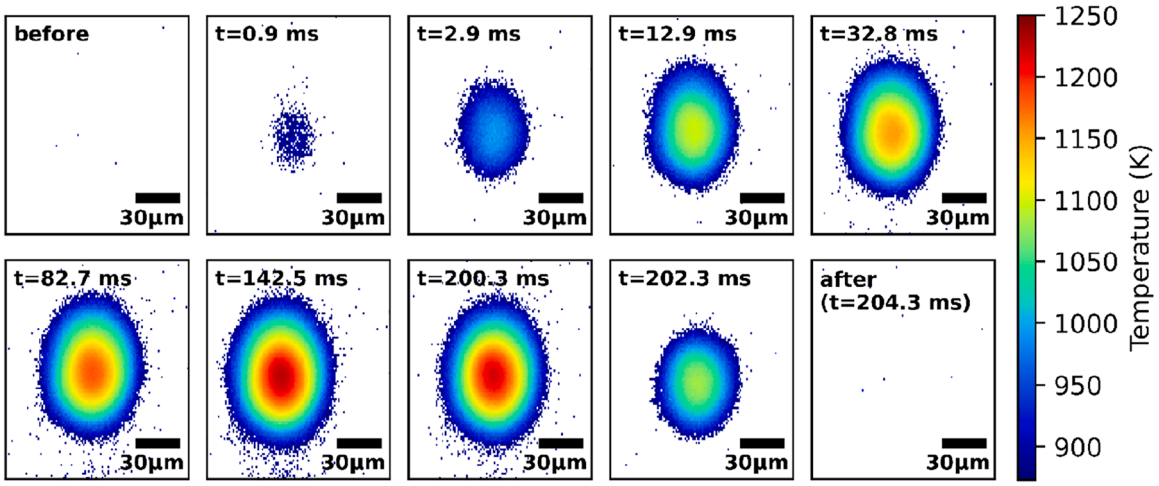

Fig. 2. False color images of the sintering spot during a 200 ms laser pulse that are recorded with a framerate of 500 fps (exposure time of 1.994 ms) by NIR high-speed thermal imaging. The images show the evolution of the surface temperature of the irradiated nanoparticle film. White color represents temperatures below 873 K. The time t refers to the elapsed time after opening of the laser shutter.

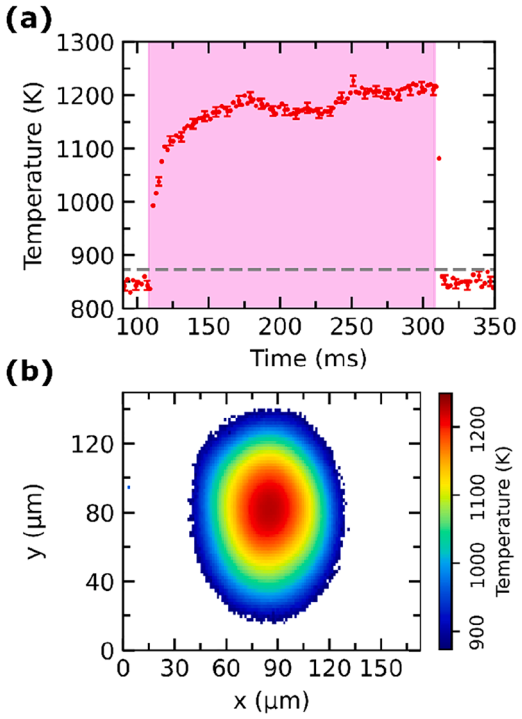

Fig. 3. (a) The temporal evolution of the hot-spot temperature. The laser shutter opens at $t = 108$ ms and closes at $t = 308$ ms. The temperatures below the grey dashed line are not real but are generated by dark noise and are displayed only to illustrate the temporal evolution. Only every forth error bar is shown for clarity. The laser pulse length is illustrated as violet area. (b) shows the temporal averaged temperature field from $t = 131$ ms (after steep temperature increase) until one frame before shutter closing, which illustrates the lateral expansion of the hot-zone. Temperatures below 873 K are shown as white pixels.

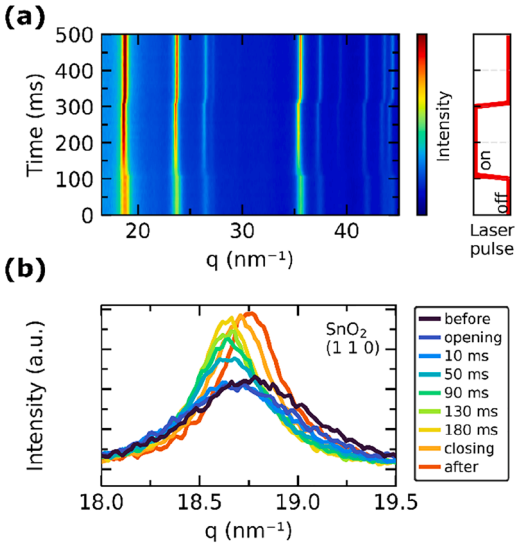

Fig. 4. (a) Waterfall representation of the time-resolved diffraction patterns for a 200 ms laser pulse. The diffractograms are recorded with a framerate of 100 fps. The laser pulse duration is displayed on the right side. (b) An enlarged view of the (110) reflection, showing its temporal evolution during laser-induced heating.

lower scattering vectors. In addition, the width of the reflections becomes progressively narrower, accompanied by an increase in the maximum intensity, which is attributed to thermally activated crystal (grain) growth by diffusion.

These effects become more pronounced when individual reflections are examined in detail. Fig. 4(b) shows the evolution of the (110) reflection during laser irradiation. A clear shift of the reflection towards lower q values is observed within the first 10 ms immediately after the laser is switched on, indicating a rapid increase in temperature observed via thermal expansion. After the first temperature increase, the reflection position remains relatively constant, suggesting that a steady-state temperature is reached. During this phase, a continuous narrowing of the shape of the Bragg reflections is observed, accompanied by an increase in the maximum intensity, which can be attributed to grain growth. After the end of the laser pulse (about 200 ms), the position of the reflections rapidly returns to the initial state, indicating a very fast cooling of the sample.

Fig. 5 displays the extracted parameter values from the Rietveld refinement of the measurement series. Rietveld refinements are performed using the software Profex [36] and a structure model of rutile-type SnO_2 (cassiterite) [37]. As shown in Fig. S. 11, the batch refinement provides reliable fits for the present material system and exposure time. For clarification, the time during the laser pulse (108 ms – 308 ms) is highlighted in violet. Fig. 5(a) shows the surface

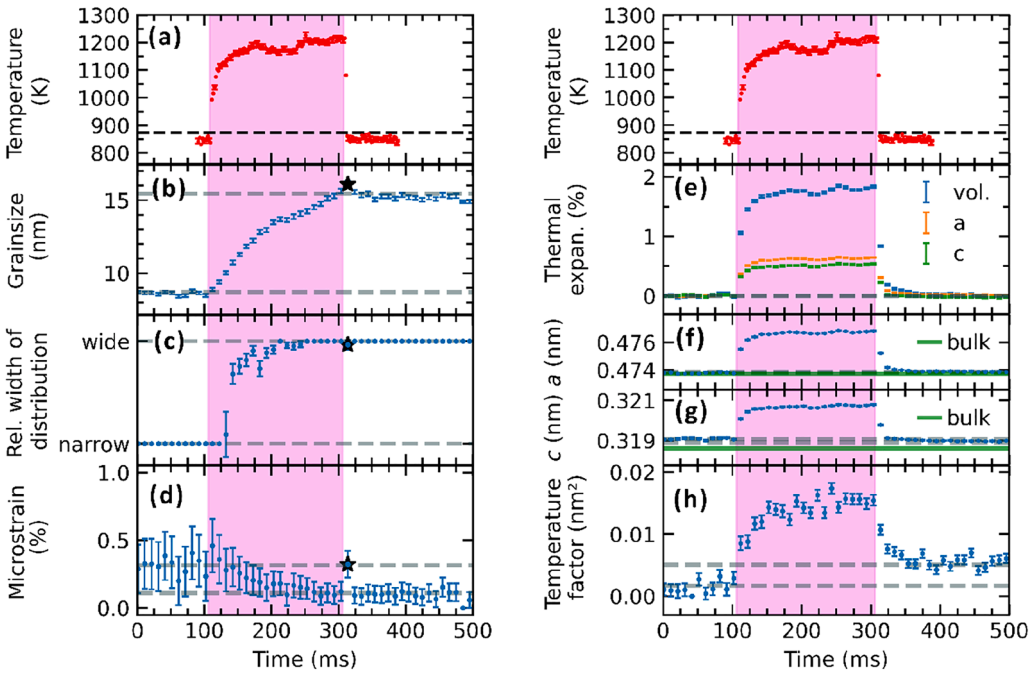

Fig. 5. Thermal and structural dynamics during a 200 ms laser pulse, offering direct correlations between the temperature-time profile and the structural transformations. The laser pulse duration is highlighted in violet. The dashed black lines in the top panels display the lower end of the thermal calibration. Values below are not physical and just shown for temporal clarity. The initial values and the values long after the laser pulse are indicated by dashed grey lines. The values, which are marked by a black star, are not reliable due to rapid cooling. The rapid cooling induces a shift of the position of the reflections within one frame and, therefore, generates a distorted line shape of the reflections.

temperature measured by the NIR high-speed camera, enabling a direct correlation with the evolving structure.

The grain size increases continuously during the laser pulse [Fig. 5 (b)], with a slight change in the middle of the pulse. The grain growth starts immediately after the steep temperature increase and the slight dip in the temperature profile is also reflected in the growth rate, indicating that it is directly coupled to temperature. The grain size starts at 8.6 nm and reaches 15.4 nm during the 200 ms laser pulse, which corresponds to a growth of 79 % and a grain size volume increase of about 475 %.

Fig. 5(c) shows a parameter representing a measure of the relative width of the grain size distribution, derived from the refinement of the reflection profile in Profex [38]. It is a qualitative indicator of the width of the grain size distribution. Prior to the laser pulse, the distribution is narrow, as typically observed for CVS-generated nanoparticles [33]. During the laser pulse, the relative standard deviation increases rapidly, indicating a broadening of the grain size distribution. Broadening during sintering is expected, even when the initial particles exhibit a narrow size distribution, since the grain sizes evolve toward a self-preserving size distribution [39–41]. Additionally, the distribution may appear broader due to the spatial intensity profile of the laser, which leads to a certain temperature distribution within the X-ray beam size.

The microstrain decreases from about 0.31 to 0.11 [Fig. 5(d)] probably due to healing of point defects. The level of microstrain is consistent with values reported for comparable SnO_2 particles with similar particle sizes determined *ex situ* [34].

Fig. 5(e) depicts the thermal expansion of the unit cell and, consequently, of the crystallites during laser heating. The unit cell volume, calculated from the lattice parameters a and c ($a \times a \times c$), closely follows the measured temperature-time profile. The volume increases already within the first frame after the shutter is opened. This behavior is consistent with the characteristic timescale of lattice expansion upon heating via electron–phonon coupling, which occurs in the picosecond regime [42], and is therefore well below the temporal resolution of the experiment. Within the first three frames it increases to about 1.8 %, followed by a period where it is relatively constant, supporting the observation of a quasi-steady state temperature. After the laser pulse is switched off, the expansion rapidly decreases to approximately 0.2 % within two frames and gradually returns to the initial state. This behavior highlights the dynamic temperature response of the locally heated sample.

The lattice parameters a and c [Fig. 5(f) and (g)] increase with temperature and closely follow the temperature evolution, as already seen in the thermal expansion. Besides the thermally induced expansion, changes in the lattice constants driven by grain growth are observed. Whereas a is already close to the bulk value at the beginning of the experiment, c is initially stretched and tends towards the bulk value during laser irradiation, also consistent with *ex situ* characterisations of comparable SnO_2 nanoparticles [34]. The temperature driven (reversible) expansion of the lattice constants is significantly larger than the changes caused by grain growth.

The temperature factor B (corresponds to the isotropic Debye-Waller factor, $B = 8\,\pi^2 <u^2>$, where $<u^2>$ is the mean square displacement [38]) for the Sn atom [Fig. 5(h)] exhibits a similar trend as the thermal expansion of the lattice parameters; however, in contrast to the lattice expansion, it does not fully return to its initial value after the laser pulse but remains slightly increased. This behavior is not fully understood. The Debye–Waller factor is expected to decrease with increasing particle size and decreasing defect concentration, as indicated by the reduction of the microstrain. Thus, the persistently elevated temperature factor may arise either from the strong quenching of defects during the rapid cooling or from an artefact caused by a temperature distribution within the X-ray beam sampling volume, which may result in particle fractions at different stages of structural evolution.

Overall, the time-resolved analysis of the thermal and structural dynamics reveals the direct correlation between temperature and crystal structure evolution. The data show a rapid heating phase followed by a relatively constant temperature during the laser pulse, accompanied by continuous grain growth and a decrease in microstrain. The unit cell volume expands by nearly 2 % due to laser-induced heating, and the

initially elongated lattice parameter *c* tends towards the bulk value. The dispersity in grain size increases, as expected during sintering. After the shutter is closed, the sample cools down within a few milliseconds. The structural parameters extracted from the *in situ* measurements are in good agreement with *ex situ* measurements of comparable SnO_2 particles.

Simultaneously with the WAXS measurements, time-resolved SAXS profiles are recorded to probe the microstructural evolution on the particulate level during laser sintering. The SAXS measurements are recorded at the same frame rate (100 fps) as the WAXS data to enable direct correlation between changes in micro- and crystal structure. Fig. 6 (a) presents the background-subtracted SAXS intensity profiles in double-logarithmic representation.

The investigated material consists of CVS-generated nanoparticles, which are dispersed by ultrasonication and deposited onto Kapton substrates via drop-casting to form thin films. Gas-phase synthesized nanoparticles typically exhibit a certain degree of polydispersity and hierarchical organization due to agglomeration [33], resulting in multiple structural levels (primary particles and agglomerates). Such hierarchical structures are well reflected in SAXS profiles [43–45].

Prior to the laser pulse, a 'knee' like Guinier regime is observed in the low-*q* area at about *q* of 5×10^{-1} nm^{-1} of the SAXS profile, which can be attributed to the primary particles. The background subtracted SAXS profile of the thin film is similar in this *q* range to the profiles observed for dispersed and comparable SnO_2 nanoparticles [46,47]. Upon laser exposure, the SAXS profile immediately changes: The "knee" shifts to smaller *q*-values and the forward scattering intensity continuously increases, indicating the growth of the primary particles into larger structures.

During laser irradiation, the 'knee' progressively shifts towards smaller *q*, indicating a growth of the primary particles. After the laser pulse the position of the 'knee' is at a *q* of approximately 1×10^{-1} nm^{-1}. Furthermore, the SAXS profile exhibits less pronounced structural features, likely as a result of increasing polydispersity, which is consistent with the WAXS results.

The evolution of the radius of gyration (R_g) is particularly evident in the Kratky plot ($q^2 \cdot I(q)$ vs q; Fig. 6(b)). At the onset of the laser pulse, the maximum shifts abruptly toward lower *q*-values, followed by a continuous shift to even lower *q* as long as the shutter remains open. Since the position of the maximum q_{max} in the Kratky plot can be directly related to R_g when spherical particles are assumed, this shift indicates a rapid increase in characteristic particle size. The temporal evolution of R_g [Fig. 7(a)] is determined according to formula [48,49]:

$$R_g \approx \frac{\sqrt{3}}{q_{max}}. \quad (1)$$

Assuming polydisperse spherical particles, a volume-weighted particle size distribution D_v (d) can be calculated from the scattering intensity profile using an Indirect Fourier Transformation (IFT) approach [50–52]. Fig. 6(c) shows the evolution of the calculated particle size distribution during laser sintering. For this analysis, the software GNOM from the ATSAS package was used [53].

Since the model of polydisperse spheres represents an approximation and the particles are strongly agglomerated, the resulting particle size distribution is not a unique solution. Therefore, it should be interpreted as a general trend rather than the exact particle size distribution. Due to agglomeration and limited *q*-range, a maximum particle diameter D_{max} cannot be uniquely determined, which may lead to oscillations in the calculated distribution [54].

Nonetheless, two main trends are observed. First, the mode of the distribution shifts toward larger particle sizes. Second, the size distribution broadens, evidenced by a decreasing amplitude and concurrent

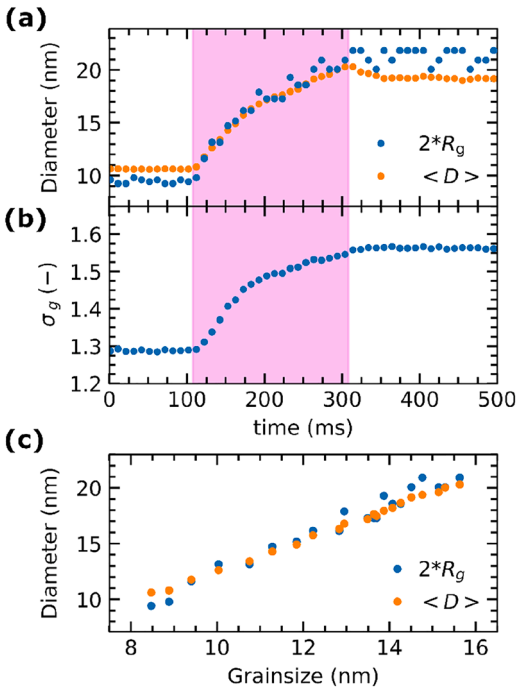

Fig. 7. Results of the analysis of the volume-weighted particle size distributions using a lognormal distribution function. (a) Temporal evolution of the extracted mean diameters $\langle D \rangle$ and of $2*R_g$, calculated from the maximum in the Kratky-plot. (b) The geometric standard deviation σ_g. The laser pulse duration (200 ms) is highlighted in violet. (c) The mean diameter $\langle D \rangle$ and $2*R_g$ plotted against the grain size determined by WAXS.

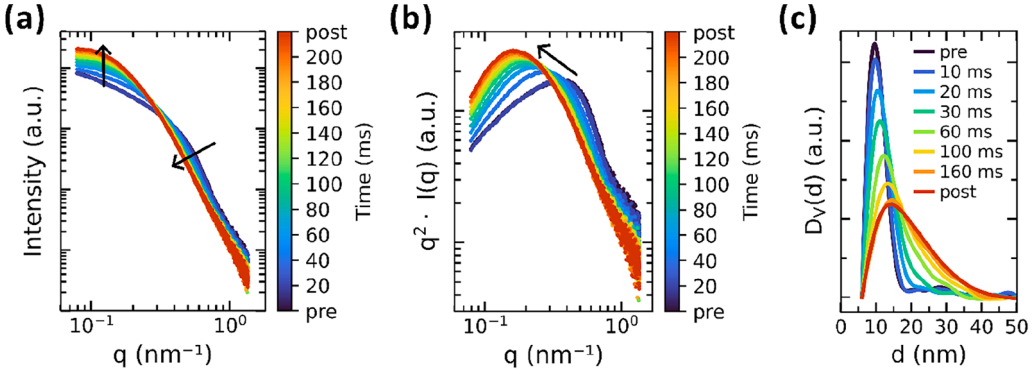

Fig. 6. (a) Double-logarithmic plot of the evolution of the SAXS profile (background subtracted) during a 200 ms laser pulse. (b) Corresponding Kratky plot, indicating the growth of R_g. (c) Extracted volume weight particle size distributions. The distributions are calculated by Indirect Fourier Transformation using the software GNOM. For clarity, not all the profiles and distributions are shown.

broadening of the right side of the mode, indicating an increased degree of polydispersity.

This observation is in agreement with the WAXS results and consistent with theoretical expectations, since during sintering the particle size distribution tends to evolve into a self-preserving size distribution [39–41], provided that no abnormal grain growth occurs. Variations in packing density and particle coordination number within the green body lead to heterogeneous growth behaviour [4], and thus to a broadening of the particle size distribution.

Furthermore, ongoing neck growth probably contributes to the determined broadening. Once a sintering neck between two particles exceeds a certain size, the connected particles will scatter coherently and are no longer detected as two separate objects but rather as a single, larger and elongated object. An apparently polydisperse distribution results if this occurs only for a fraction of the particles while others remain separated.

Additionally, variations in laser intensity and the resulting temperature gradients within the X-ray probed region may contribute to the observed broadening of the distribution. However, no residual fraction of the primary particle-size class is observed after laser treatment. This observation further supports the conclusion that the laser-heated region exceeds the X-ray sampling volume, spatially overlaps with it, and extends throughout the entire film thickness. As a result, all nanoparticles probed by the X-ray beam are heated sufficiently to undergo grain growth. In general, the magnitude of the broadening appears to be in line with expectations.

Fig. 7a shows the evolution of the diameter of gyration, i.e. 2 R_g, and the volume weighted mean diameter $\langle D \rangle$ derived from a lognormal fit of the particle size distribution. The diameter of gyration and $\langle D \rangle$ follow a comparable pattern. Fig. 7(b) displays the geometric standard deviation of the corresponding particle size distribution. The initial value of σ_g is around 1.29 before the laser irradiation, which is within the typical range for CVS synthesized nanoparticles [33,47].

During laser irradiation σ_g increases to 1.56, due to broadening discussed before. The change in the increase of the particle diameter (at a sintering time of about 180 ms), as well as in the grain size, is also reflected in the evolution of σ_g. Overall, the evolution of the particle size distribution indicates primary particle growth, evidenced by the increase in $\langle D \rangle$, and a broadening of the distribution as seen by increasing σ_g. In Fig. 7(c) $\langle D \rangle$ and $2 \bullet R_g$ are plotted against the grain size determined by WAXS. For both quantities, a linear relationship is observed, confirming that SAXS at this q-range probes the diameter of the primary particles rather than the pores or other structural features. Moreover, the analysis using indirect Fourier transformation provides consistent and reasonable results for $\langle D \rangle$. Although, both the ratio of the initial particle sizes and the slope of the linear relationship are greater than 1.

3.3. Microstructural and particle evolution during different pulse length

Fig. 8 compares the structural evolution during laser irradiation with different pulse durations. At the onset of the laser pulses, very similar trends are observed across all measurements, as reflected in the thermal evolution, grain, and particle growth. The temperature rises within the first 30 to 40 ms, after which a quasi-steady-state temperature is established. However, due to the highly localized heating, the local heat balance evolves dynamically by local structural heterogeneities within the sample, resulting in slightly different temperature profiles.

Toward the end of the 100 ms laser pulse, a sudden and pronounced temperature increase is observed. This effect is likely caused by a local delamination of the nanoparticle film from the substrate. Since the substrate acts as an efficient heat sink, in contrast to the porous nanoparticle film where heat is partially retained, such a detachment would significantly alter the local thermal balance.

Grain and particle growth become measurable approximately one frame (10 ms) after the onset of thermal expansion and small temperature variations are directly reflected in changes in the lattice expansion

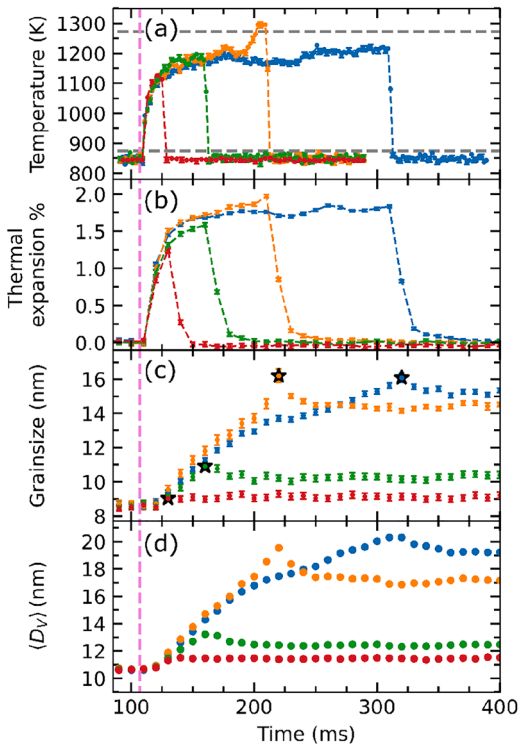

Fig. 8. Comparison of four different laser pulses (20 ms, 50 ms, 100 ms, 200 ms). It is shown the temperature-time profile (a), the thermal expansion (b) and the evolution of the grain size (from WAXS) (c) as well as volume-weighted mean particle diameter (d), as determined by SAXS. The opening time of the laser shutter (at about 108 ms) is indicated by a dashed violet line. The dashed grey lines in the top panel reveal the calibrated temperature range. Below and above the grey lines the temperatures are not physical and just shown for clarity.

as well as in the structural evolution. Notably, at the end of each laser pulse, a transient increase in grain and particle size is observed, which gradually relaxes toward the final state. This is probably caused by the rapid cooling, which forces a very fast structural relaxation and therefore high residual stresses which are relieved by mechanically relaxation after cooling.

Fig. 9 presents SEM images of the resulting microstructures within the sintering spots after irradiation with different laser pulse durations, alongside the unsintered SnO_2 nanoparticulate film. The figure thus illustrates the time-dependent microstructural evolution during laser sintering.

The unsintered green body (nanoparticulate SnO_2 film on a polyimide substrate) consists of agglomerated nanoparticle clusters with a high porosity and a broad pore size distribution. After a 20 ms laser pulse, no distinct particle growth is visible. The powder bed appears slightly more compact. However, this observation may be influenced by sampling variations.

Following a 50 ms pulse, a pronounced increase in particle size is evident. It is accompanied by a morphological evolution of the particle clusters, characterized by clearly visible sinter necks between adjacent particles. After a 100 ms laser pulse, parts of the aggregates exhibit a more elongated or rod-like shape. In some regions, previously formed sinter necks appear reduced or absent, possibly due to grain boundary migration. Larger voids between aggregates are formed, which may result from mass transport from the surface toward the interior of the film.

For a 200 ms pulse, continued particle growth is apparent, and the particle network appears more compact and consolidated. The pore size decreased, compared to the 100 ms pulse, although a high a degree of porosity still remains. Overall, the observed microstructures closely

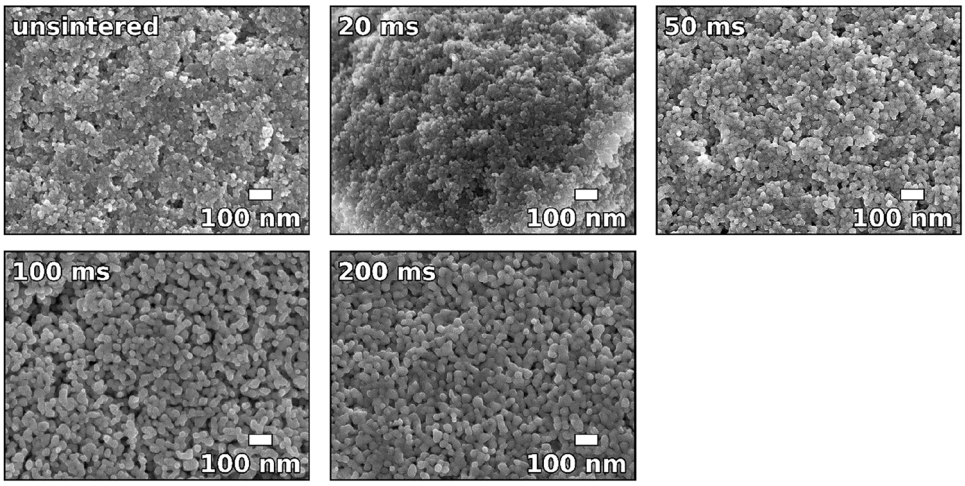

Fig. 9. SEM images of the unsintered SnO_2 nanoparticle film and the sintering spots after irradiation with laser pulses of 20 ms, 50 ms, 100 ms, and 200 ms. The images are recorded *ex situ* after a coating with 8 nm carbon film, for better image quality by minimizing charging effects.

resemble those typically reported [55] for the initial stages of sintering in highly porous compacts with relatively low (green) densities of approximately 40 % of the bulk density.

The results show that forming dense nanocrystalline materials from SnO_2 nanoparticles is difficult, even under the applied (ultra)fast firing conditions characterized by very high heating rates, elevated temperatures, and short sintering times. This observation is consistent with previous studies reporting that pure SnO_2 hardly densifies during pressureless sintering [56–58].

3.4. Kinetics of grain growth

Isothermal normal grain growth in the absence of pinning forces can be described by a power law relationship [59,60]:

$$D^n - D_0^n = k\ (t - t_0), \tag{2}$$

where D and D_0 are the mean grain sizes at time t and the initial time t_0, n is the grain growth exponent and k is a temperature dependent rate constant. Originally, the grain growth exponent $n = 2$ was derived for pure materials under idealized conditions [59]. However, experimental studies have consistently reported higher values of n, typically between 2 and 4, reflecting additional kinetic constraints [61,62]. Insights into the dominant diffusion mechanism may be concluded directly from the measured grain growth exponent [63,64], according to the classical Herring-scaling-law [65].

The rate constant k can be used to determine an effective activation energy for the governing growth process if data at different temperatures are available.

Fig. 10(b) presents the temporal evolution of the grain size together with fits according to Eq. (2) for the 100 ms and 200 ms laser pulse during the time, where the temperature approaches quasi-isothermal conditions. In addition, both the instantaneous temperature profiles and the mean temperatures within the fitting interval are shown as dashed lines. The shorter laser pulses (20 ms and 50 ms) are excluded from the analysis, as no isothermal growth regime is established in these cases.

Table 1 summarizes the fitting parameters and the corresponding mean temperatures, including the standard error of the mean temperature.

The obtained values of the growth exponent n range between 3.3 and 4.6 (Table 1). Since sintering can be considered to be in the initial stage, the growth process is mostly pore-controlled, as pores act as the rate-limiting factor while grain boundaries are largely immobile. Under these conditions, grain growth is expected to occur by diffusion or vapor transport mechanisms. An exponent of $n = 3$ may indicate lattice diffusion or gas-phase transport as the dominant mechanism, whereas $n = 4$ is commonly associated with surface diffusion [63,66].

For nanocrystalline SnO_2 a limiting grain size has been observed experimentally, at which grain growth stagnates. Such growth

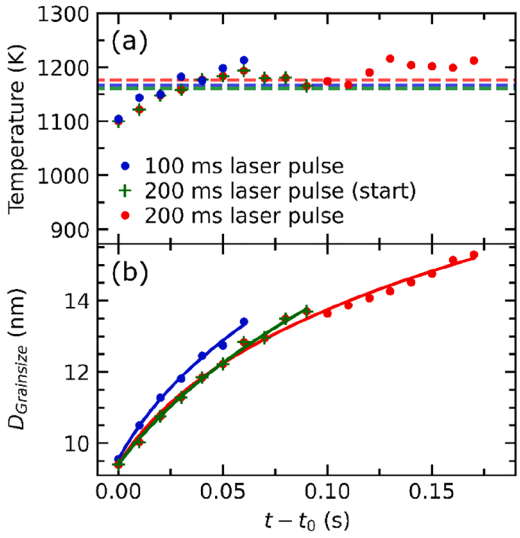

Fig. 10. (a) Temperature during the quasi-isothermal period under laser irradiation and the temporal mean temperature. (b) The evolution of the grain size together with a kinetic fit according to the isothermal normal grain growth model.

Table 1
Kinetics of grain growth obtained from WAXS during laser sintering. Given are the mean temperature and the standard error of the mean, the grain growth exponent n and the rate constant k for different laser pulses. The values are obtained by least-square fitting of Eq. (2).

	Temperature (K)	Grain growth exponent n	Rate constant k (m^n /s)
100 ms laser pulse	1167 (13) K	3.8 (5)	$(1 \pm 6)\ 10^{-29}$
200 ms laser pulse (up to t-t_0 =100 ms, green crosses)	1161 (9) K	3.3 (3)	$(2 \pm 8)\ 10^{-25}$
200 ms laser pulse	1176 (7) K	4.6(3)	$(1 \pm 6)\ 10^{-35}$

saturation can lead to artificially high and deviant apparent n values when fitting the classical growth law [67–69]. In these cases, a direct physical interpretation of n becomes ambiguous.

In the present case, the interpretation of n must likewise be treated with caution due to the extremely short sintering times, the relatively small differences in grain size, and the evolving temperature profile during laser irradiation. Nevertheless, the obtained values still provide qualitative insight into the dominant mass transport processes. The magnitude of n suggests that multiple diffusion mechanisms may contribute to the grain growth kinetics, with surface diffusion potentially playing a dominant role [70]. This interpretation is consistent with the limited densification observed in the microstructural analysis (SEM), as surface diffusion promotes coarsening without significant pore elimination.

For the 200 ms laser pulse, a possible transition in the dominant mechanism may be indicated by the evolution of the fitted exponent. An initial fit up to $t - t_0 = 100$ ms yields $n = 3.27$ (Fig. 10 green data set), whereas fitting over a longer time interval ($t - t_0 = 174$ ms) results in $n = 4.56$. This apparent shift is also reflected in the evolution of other structural parameters, suggesting a change in the governing kinetics during the later stages of the process. The particle growth observed by SAXS (Fig. 6 and Fig. 7) was also analyzed for the 200 ms laser pulse (Fig. S. 12). The analysis reveals a particle-growth exponent of n ≈ 4 (Table S. 1), suggesting surface diffusion as the dominant mass-transport mechanism. The magnitude of the exponent agrees with the grain-growth behavior extracted from the WAXS data. This finding is consistent with the strong linear correlation between the mean particle size and grain size shown in Fig. 7(c). Since the slope of the linear fit is greater than unity, the rate constants differ despite identical growth exponents.

A determination of the activation energies would require longer isothermal processing times at a wider span of temperatures and a consideration of the limiting grain size [67].

3.5. Thermal expansion due to laser induced heating

Fig. 5 exhibits the time-resolved evolution of the unit-cell volume (Fig. 5e), the lattice constants, and the thermal evolution of the SnO_2 particles during laser irradiation. A pronounced expansion of both lattice parameters and the unit-cell volume is observed, closely correlated with the temporal evolution of the temperature. In contrast, lattice changes associated with crystal growth remain negligible compared to the dominant and reversible thermal expansion.

A nearly linear increase in the lattice constants with temperature is observed in the range between 900 and 1300 K when the lattice constants determined during laser-induced heating are plotted as a function of temperature (Fig. 11). However, the linear fit does not reproduce the lattice parameters at room temperature. In literature [71,72], the observed values for the expansion coefficient differ, and different expansion coefficients are observed for nanoparticles and bulk SnO_2. The expansion coefficients determined in this study are higher than the reported values.

It has been reported [71] that the thermal expansion of SnO_2 is not linear across the entire temperature range, but rather exhibits temperature-dependent variations in slope close to room temperature. Such behavior at the elevated temperatures accessed in the present time-resolved measurements could explain differing values and the mismatch of the lattice constant at room temperature. The thermal expansion values determined here (Table 2) are in good agreement with data of an *in situ* study of a gas-phase synthesis of SnO_2 nanoparticles at comparable temperatures [73].

4. Conclusion

The structural evolution of SnO_2 nanoparticles during resonant laser sintering is investigated by combining time-resolved *in situ* and *operando* SAXS and WAXS with high-speed NIR thermography. This approach enables the simultaneous observation of micro- and crystal structure dynamics together with the evolution of the temperature field during processing. A time resolution of 10 ms in the X-ray scattering experiments proved suitable for resolving particle and crystallite dynamics during the process, while temperatures are measured with frame rates of up to 500 fps.

The correlation of the temperature–time profile with the structural evolution reveals the direct coupling between the transient temperature field and the microstructural dynamics during resonant laser sintering. The lattice expansion follows the temperature evolution almost instantaneously, while grain growth and particle growth become observable in the second frame, about 20 ms after shutter opening. Variations in the transient temperature field are directly reflected in the structural response, affecting the growth rates on both the micro- and crystal structure level, as well as the lattice expansion, the evolution of microstrain, and the Debye–Waller factor.

The analysis shows that particle growth is driven by grain growth caused by diffusive processes, where surface diffusion is most likely dominant. The development of elongated particle structures and a broadening of the particle size distribution suggests grain boundary motion at laser durations longer than 50 ms.

The lattice expansion during laser heating is quantified, enabling an estimation of the thermal expansion coefficient of SnO_2 in the temperature range between approximately 900 K and 1300 K (isotropic average of about $11 \cdot 10^{-6}$ / K). This may be used as additional probe for directly measuring the temperature of the heated particles.

Despite the extreme heating rates and short processing times, densification of the nanoparticle films remains limited, while substantial grain growth and particle coarsening occur. This observation highlights

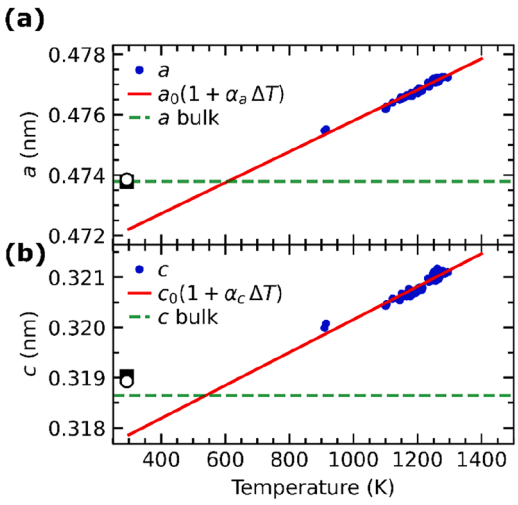

Fig. 11. Thermal expansion of the lattice constants during laser induced heating. In blue are shown the lattice constants that are determined by Rietveld refinement of *in situ* WAXS measurements during laser pulses. The temperatures are measured by NIR high-speed thermography. The starting values of the lattice constants are shown as black squares and the lattice constants after the laser pulse are shown as black open circles.

Table 2
Thermal expansion coefficients that are determined by linear approximation of the lattice constants. The lattice constants are measured *in situ* during the laser induced heating.

Lattice constants	Expansion coefficient α (10^{-6} / K)	y-intercept (at $T = 0$ K) (nm)
a	10.9 (3)	0.4707(2)
c	10.4 (4)	0.3169(2)

the intrinsic difficulty of achieving significant densification of pure SnO_2 nanoparticle compacts during pressureless sintering.

Overall, the present results demonstrate that time-resolved X-ray scattering combined with fast thermal imaging provides a powerful tool to directly observe particle, lattice, and thermal dynamics during (ultrafast) laser sintering, enabling mechanistic insight into microstructural evolution under highly transient processing conditions.

Funding

Open Access funding enabled and organized by project DEAL. Work was funded by the German Research Foundation (DFG) through project 'Reactive Laser-Sintering for generation of Copper-Aluminum-Oxide from nanoscaled powders: Optimization of process conditions and investigation of mechanisms' (SCHR 1753/1-1, WI 981/19-1). The high-speed camera and optics were funded through project SPP 1959/1 (Schwerpunktprogramm), 'Manipulation of Matter controlled by electric and magnetic fields: Towards novel synthesis and processing routes of inorganic materials' (WI 981/16). The X-ray data of the pristine SnO_2 powder was collected using the Rigaku Smartlab High Resolution X-ray diffractometer, funded through the DFG (German Research Foundation) Instrument proposal INST 20876/395-1 FUGG and the state of North Rhine-Westfalia, Germany.

CRediT authorship contribution statement

Jeldrik Schulte: Writing – original draft, Visualization, Validation, Methodology, Investigation, Formal analysis, Data curation, Conceptualization. **Markus Winterer:** Writing – review & editing, Validation, Supervision, Resources, Methodology, Investigation, Funding acquisition, Conceptualization. **Martin A. Schroer:** Writing – review & editing, Validation, Supervision, Methodology, Investigation, Funding acquisition, Conceptualization.

Declaration of competing interest

The authors declare that they have no known competing financial interests or personal relationships that could have appeared to influence the work reported in this paper.

Acknowledgements

The authors gratefully acknowledge the German Research Foundation (DFG) for funding through project 'Reactive Laser-Sintering for generation of Copper-Aluminum-Oxide from nanoscaled powders: Optimization of process conditions and investigation of mechanisms' (SCHR 1753/1-1, WI 981/19-1) and SPP 1959/1 (Schwerpunktprogramm), 'Manipulation of Matter controlled by electric and magnetic fields: Towards novel synthesis and processing routes of inorganic materials' (WI 981/16). We gratefully acknowledge DESY (Hamburg, Germany), a member of the Helmholtz Association HGF, for the provision of experimental facilities. Parts of this research were carried out at PETRA III. Data were collected using beamline P62 (SAXSMAT) operated by DESY Photon Science. We would like to thank Dr. Xiao Sun and Dr. André Conceição for excellent assistance during the experiments. Beamtime was allocated for proposals I-20230897 and I-20240729. Moreover, we thank Dr. Sasa Lukic for providing the SnO_2 particles. Finally, the authors would like to acknowledge Shradha R. Joshi for excellent support during the beam time, as well as Florian Kinzel, Maximilian Stepponat and Robert Rahtz for their great support in the laboratory.

Supplementary materials

Supplementary material associated with this article can be found, in the online version, at doi:10.1016/j.actamat.2026.122527.

Data availability

The datasets used and/or analyzed during the current study are available from the corresponding author on reasonable request.

References

[1] T.H. Becker, P. Kumar, U. Ramamurty, Fracture and fatigue in additively manufactured metals, Acta Mater. 219 (2021) 117240, https://doi.org/10.1016/j.actamat.2021.117240.
[2] J.E. Burke, Ceramics today, Science 161 (1968) 1205–1212, https://doi.org/10.1126/science.161.3847.1205.
[3] M. Biesuz, T.H. de Beauvoir, E. de Bona, M. Cassetta, C. Manière, V.M. Sglavo, C. Estournès, Ultrafast high-temperature sintering (UHS) vs. conventional sintering of 3YSZ: microstructure and properties, J. Eur. Ceram. Soc. 44 (2024) 4741–4750, https://doi.org/10.1016/j.jeurceramsoc.2024.01.064.
[4] M.N. Rahaman, Ceramic Processing and Sintering, 2nd ed., CRC Press, Boca Raton, 2003.
[5] I.W. Chen, X.H. Wang, Sintering dense nanocrystalline ceramics without final-stage grain growth, Nature 404 (2000) 168–171, https://doi.org/10.1038/35004548.
[6] S.C. Liao, W.E. Mayo, K.D. Pae, Theory of high pressure/low temperature sintering of bulk nanocrystalline TiO_2, Acta Mater. 45 (1997) 4027–4040, https://doi.org/10.1016/S1359-6454(97)00087-6.
[7] Z. Guo, R.I. Todd, Acceleration of grain boundary diffusion during ultra-fast firing (UHS) of alumina powder compacts, Acta Mater. 282 (2025) 120471, https://doi.org/10.1016/j.actamat.2024.120471.
[8] H. Gleiter, Nanostructured materials: basic concepts and microstructure, Acta Mater. 48 (2000) 1–29, https://doi.org/10.1016/S1359-6454(99)00285-2.
[9] E. Arzt, Size effects in materials due to microstructural and dimensional constraints: a comparative review, Acta Mater. 46 (1998) 5611–5626, https://doi.org/10.1016/S1359-6454(98)00231-6.
[10] A.J. Allen, G.G. Long, H.M. Kerch, S. Krueger, G. Skandan, H. Hahn, J.C. Parker, Sintering studies of nanophase ceramic oxides using small angle scattering, Ceram. Int. 22 (1996) 275–280, https://doi.org/10.1016/0272-8842(96)84747-X.
[11] A. Sandmann, C. Notthoff, M. Winterer, Continuous wave ultraviolet-laser sintering of ZnO and TiO_2 nanoparticle thin films at low laser powers, J. Appl. Phys. 113 (2013), https://doi.org/10.1063/1.4788906.
[12] H. Palneedi, J.H. Park, D. Maurya, M. Peddigari, G.-T. Hwang, V. Annapureddy, J.-W. Kim, et al., Laser irradiation of metal oxide films and nanostructures: applications and advances, Adv. Mater. 30 (2018) e1705148, https://doi.org/10.1002/adma.201705148.
[13] M. Kermani, C. Hu, S. Grasso, From pit fire to Ultrafast high-temperature sintering (UHS): a review on ultrarapid consolidation, Ceram. Int. 49 (2023) 4017–4029, https://doi.org/10.1016/j.ceramint.2022.11.091.
[14] L. Song, J. Ma, Q. Zhang, Z. Shen, Laser melted oxide ceramics: multiscale structural evolution with non-equilibrium features, J. Materiom. 5 (2019) 436–445, https://doi.org/10.1016/j.jmat.2019.02.003.
[15] S. Das, Physical aspects of process control in selective laser sintering of metals, Adv. Eng. Mater. 5 (2003) 701–711, https://doi.org/10.1002/adem.200310099.
[16] J. Mazumder, S. Sircar, C. Ribaudo, A. Kar, New materials: non-equilibrium synthesis by laser, J. Laser Appl. 1 (1989) 27–42, https://doi.org/10.2351/1.4745227.
[17] V. Mackert, J.S. Gebauer, C. Notthoff, M. Winterer, Zinc stannate by reactive laser sintering, Appl. Surf. Sci. 457 (2018) 1174–1180, https://doi.org/10.1016/j.apsusc.2018.06.304.
[18] V. Mackert, J.S. Gebauer, D. Tzolov, J. Schulte, A. Sandmann, M. Winterer, Optimizing nanoparticles from the gas phase for dispersions and inks for printed electronics, Powder Technol. 478 (2026) 122518, https://doi.org/10.1016/j.powtec.2026.122518.
[19] S.K. Garlapati, J.S. Gebauer, S. Dehm, M. Bruns, M. Winterer, H. Hahn, S. Dasgupta, Room-temperature processing of printed oxide FETs using ultraviolet photonic curing, Adv. Elect. Mater. 3 (2017), https://doi.org/10.1002/aelm.201600476.
[20] K.K. Singh, A. Wakai, A. Moridi, Advancements in operando X-ray techniques for metal additive manufacturing, Commun. Mater. 5 (2024), https://doi.org/10.1038/s43246-024-00699-7.
[21] P. Shyam, F.H. Gjørup, M.I. Mørch, A.P. Laursen, A.Z. Eikeland, I. Kantor, M. R. Jørgensen, et al., Sintering in seconds, elucidated by millisecond in situ diffraction, Appl. Mater. Today 35 (2023) 101960, https://doi.org/10.1016/j.apmt.2023.101960.
[22] C. Kenel, D. Grolimund, J.L. Fife, V.A. Samson, S. van Petegem, H. van Swygenhoven, C. Leinenbach, Combined in situ synchrotron micro X-ray diffraction and high-speed imaging on rapidly heated and solidified Ti–48Al under additive manufacturing conditions, Scr. Mater. 114 (2016) 117–120, https://doi.org/10.1016/j.scriptamat.2015.12.009.
[23] G. Gadikota, F. Zhang, A.J. Allen, Towards understanding the microstructural and structural changes in natural hierarchical materials for energy recovery: in-operando multi-scale X-ray scattering characterization of Na- and Ca-montmorillonite on heating to 1150 °C, Fuel (Lond) 196 (2017) 195–209, https://doi.org/10.1016/j.fuel.2017.01.092.
[24] S.R. Joshi, M.A. Schroer, M. Winterer, In Situ X-ray scattering of tin oxide nanoparticles during chemical vapor synthesis, Chem. Mater. 37 (2025) 5710–5723, https://doi.org/10.1021/acs.chemmater.5c00848.

[25] A. Lassenberger, T.A. Grünewald, P.D.J. van Oostrum, H. Rennhofer, H. Amenitsch, R. Zirbs, H.C. Lichtenegger, et al., Monodisperse iron oxide nanoparticles by thermal decomposition: elucidating particle formation by second-resolved in situ small-angle X-ray scattering, Chem. Mater 29 (2017) 4511–4522, https://doi.org/10.1021/acs.chemmater.7b01207.

[26] G. Beaucage, H.K. Kammler, R. Mueller, R. Strobel, N. Agashe, S.E. Pratsinis, T. Narayanan, Probing the dynamics of nanoparticle growth in a flame using synchrotron radiation, Nat. Mater. 3 (2004) 370–373, https://doi.org/10.1038/nmat1135.

[27] A.J. Allen, I. Levin, R.A. Maier, S.E. Witt, F. Zhang, I. Kuzmenko, In situ characterization of ceramic cold sintering by small-angle scattering 104 (2021) 2442–2448, 10.1111/jace.17664.

[28] J. Schulte, M.A. Schroer, M. Winterer, Operando high speed near infrared imaging during laser sintering of nanoparticles for time and space resolved temperature measurements, Sci. Rep. 16 (2026), https://doi.org/10.1038/s41598-026-37445-7.

[29] S. Das, V. Jayaraman, SnO_2: a comprehensive review on structures and gas sensors, Prog. Mater. Sci. 66 (2014) 112–255, https://doi.org/10.1016/j.pmatsci.2014.06.003.

[30] S.R. Mishra, M. Ahmaruzzaman, Tin oxide based nanostructured materials: synthesis and potential applications, Nanoscale 14 (2022) 1566–1605, https://doi.org/10.1039/D1NR07040A.

[31] B. Subha, R. Saravanan, N. Srinivasan, M.H.A. Suleiman, M. Selvaraj, The impact of sintering temperature on microstructure, optical and thermal properties of SnO_2 ceramics, J. Mater. Sci.: Mater. Electron. 35 (2024) 1795, https://doi.org/10.1007/s10854-024-13543-y.

[32] S. Haas, X. Sun, A.L.C. Conceição, J. Horbach, S. Pfeffer, The new small-angle X-ray scattering beamline for materials research at PETRA III: SAXSMAT beamline P62, J. Synchrotron Rad. 30 (2023) 1156–1167, https://doi.org/10.1107/S1600577523008603.

[33] M. Winterer, Nanocrystalline Ceramics, Springer, Berlin Heidelberg, Berlin, Heidelberg, 2002.

[34] V. Mackert, T. Winter, S. Jackson, R. Kalia, A. Levish, S. Lukic, J. Geiss, et al., Very small nanocrystalline tin dioxide particles: local-, crystal-, and micro-structure, J. Phys. Chem. C 127 (2023) 17389–17405, https://doi.org/10.1021/acs.jpcc.3c02110.

[35] G. Ashiotis, A. Deschildre, Z. Nawaz, J.P. Wright, D. Karkoulis, F.E. Picca, J. Kieffer, The fast azimuthal integration Python library: pyFAI, J. Appl. Crystallogr. 48 (2015) 510–519, https://doi.org/10.1107/S1600576715004306.

[36] N. Doebelin, R. Kleeberg, Profex: a graphical user interface for the Rietveld refinement program BGMN, J. Appl. Crystallogr. 48 (2015) 1573–1580, https://doi.org/10.1107/S1600576715014685.

[37] W.H. Baur, A.A. Khan, Rutile-type compounds. IV. SiO_2, GeO_2 and a comparison with other rutile-type structures, Acta Crystallogr. B 27 (1971) 2133–2139.

[38] J. Bergmann, T. Taut, Rietveld Analysis Program - BGMN. Manual, 4th ed, Dresden, 2005.

[39] R.M. German, Coarsening in sintering: grain shape distribution, grain size distribution, and grain growth kinetics in solid-pore systems, Crit. Rev. Solid State Mater. Sci. 35 (2010) 263–305, https://doi.org/10.1080/10408436.2010.525197.

[40] I. Nettleship, R.J. McAfee, W.S. Slaughter, Evolution of the grain size distribution during the sintering of Alumina at 1350 °C, J. Am. Ceram. Soc. 85 (2002) 1954–1960, https://doi.org/10.1111/j.1151-2916.2002.tb00387.x.

[41] R.M. German, Sintering Theory and Practice, Wiley, New York, Chichester, 1996.

[42] O. Ekici, R.K. Harrison, N.J. Durr, D.S. Eversole, M. Lee, A. Ben-Yakar, Thermal analysis of gold nanorods heated with femtosecond laser pulses, J. Phys. D: Appl. Phys. 41 (2008) 185501, https://doi.org/10.1088/0022-3727/41/18/185501.

[43] G. Beaucage, Approximations leading to a unified exponential/power-law approach to small-angle scattering, J. Appl. Crystallogr. 28 (1995) 717–728, https://doi.org/10.1107/S0021889895005292.

[44] G. Beaucage, D.W. Schaefer, Structural studies of complex systems using small-angle scattering: a unified Guinier/power-law approach, J. Non-Cryst. Solids 172-174 (1994) 797–805, https://doi.org/10.1016/0022-3093(94)90581-9.

[45] D.W. Schaefer, A.J. Hurd, Growth and structure of combustion aerosols: fumed silica, Aerosol Sci. Technol. 12 (1990) 876–890, https://doi.org/10.1080/02786829008959400.

[46] V. Mackert, M.A. Schroer, M. Winterer, Unraveling agglomeration and deagglomeration in aqueous colloidal dispersions of very small tin dioxide nanoparticles, J. Colloid Interface Sci. 608 (2022) 2681–2693, https://doi.org/10.1016/j.jcis.2021.10.194.

[47] V. Mackert, S. Seifert, M. Winterer, In situ probing of structure and deagglomeration of SnO_2 colloids via small-angle X-ray scattering, Powder Technol. 464 (2025) 121227, https://doi.org/10.1016/j.powtec.2025.121227.

[48] A. Deschamps, F. de Geuser, On the validity of simple precipitate size measurements by small-angle scattering in metallic systems, J. Appl. Crystallogr. 44 (2011) 343–352, https://doi.org/10.1107/S0021889811003049.

[49] F. de Geuser, A. Deschamps, Precipitate characterisation in metallic systems by small-angle X-ray or neutron scattering, C. R. Phys. 13 (2012) 246–256, https://doi.org/10.1016/j.crhy.2011.12.008.

[50] D.I. Svergun, Determination of the regularization parameter in indirect-transform methods using perceptual criteria, J. Appl. Crystallogr. 25 (1992) 495–503, https://doi.org/10.1107/S0021889892001663.

[51] D.I. Svergun, E.V. Shtykova, A.T. Dembo, L.M. Bronstein, O.A. Platonova, A. N. Yakunin, P.M. Valetsky, et al., Size distributions of metal nanoparticles in polyelectrolyte gels, J. Chem. Phys. 109 (1998) 11109–11116, https://doi.org/10.1063/1.477749.

[52] V.V. Volkov, P.V. Konarev, A.E. Kryukova, Combined scheme of reconstruction of the particle size distribution function using small-angle scattering data, Jetp Lett. 112 (2020) 591–595, https://doi.org/10.1134/S0021364020210110.

[53] K. Manalastas-Cantos, P.V. Konarev, N.R. Hajizadeh, A.G. Kikhney, M. V. Petoukhov, D.S. Molodenskiy, A. Panjkovich, et al., ATSAS 3.0: expanded functionality and new tools for small-angle scattering data analysis, J. Appl. Crystallogr. 54 (2021) 343–355, https://doi.org/10.1107/S1600576720013412.

[54] D.A. Jacques, J. Trewhella, Small-angle scattering for structural biology–expanding the frontier while avoiding the pitfalls, Protein Sci. 19 (2010) 642–657, https://doi.org/10.1002/pro.351.

[55] C. Greskovich, K.W. Lay, Grain growth in very porous Al_2O_3, Compacts 55 (1972) 142–146, https://doi.org/10.1111/j.1151-2916.1972.tb11238.x.

[56] E.R. Leite, J.A. Cerri, E. Longo, J.A. Varela, C.A. Paskocima, Sintering of ultrafine undoped SnO_2 powder, J. Eur. Ceram. Soc. 21 (2001) 669–675, https://doi.org/10.1016/S0955-2219(00)00250-8.

[57] L. Koroglu, C. Aciksari, E. Ayas, E. Ozel, E. Suvaci, A comparative study of spark plasma and conventional sintering of undoped SnO_2 sputtering targets, Mater. Chem. Phys. 290 (2022) 126624, https://doi.org/10.1016/j.matchemphys.2022.126624.

[58] R.H. Castro, G.J. Pereira, D. Gouvêa, Surface modification of SnO_2 nanoparticles containing Mg or Fe: effects on sintering, Appl. Surf. Sci. 253 (2007) 4581–4585, https://doi.org/10.1016/j.apsusc.2006.10.010.

[59] J.E. Burke, D. Turnbull, Recrystallization and grain growth, Prog. Met. Phys. 3 (1952) 220–292, https://doi.org/10.1016/0502-8205(52)90009-9.

[60] V. Novikov, On description of grain growth kinetics, Scr. Mater. 39 (1998) 945–949, https://doi.org/10.1016/S1359-6462(98)00249-8.

[61] W.D. Kingery, B. Françis, Grain Growth in Porous Compacts 48 (1965) 546–547, https://doi.org/10.1111/j.1151-2916.1965.tb14665.x.

[62] E. Hersent, K. Marthinsen, E. Nes, On the effect of atoms in solid solution on grain growth kinetics, Metall. Mater. Trans. A 45 (2014) 4882–4890, https://doi.org/10.1007/s11661-014-2459-y.

[63] H.V. Atkinson, Overview no. 65: theories of normal grain growth in pure single phase systems, Acta Metall. 36 (1988) 469–491, https://doi.org/10.1016/0001-6160(88)90079-X.

[64] X. Wang, J. Zhao, E. Cui, Z. Sun, H. Yu, Grain growth kinetics and grain refinement mechanism in Al_2O_3/WC/TiC/graphene ceramic composite, J. Eur. Ceram. Soc. 41 (2021) 1391–1398, https://doi.org/10.1016/j.jeurceramsoc.2020.10.019.

[65] C. Herring, Effect of change of scale on sintering phenomena, J. Appl. Phys. 21 (1950) 301–303, https://doi.org/10.1063/1.1699658.

[66] F.A. Nichols, Theory of grain growth in porous compacts, J. Appl. Phys. 37 (1966) 4599–4602, https://doi.org/10.1063/1.1708102.

[67] C. Shek, J. Lai, G. Lin, Grain growth in nanocrystalline SnO_2 prepared by sol-gel route, Nanostruct. Mater. 11 (1999) 887–893, https://doi.org/10.1016/S0965-9773(99)00387-6.

[68] J. Lai, C. Shek, G. Lin, Grain growth kinetics of nanocrystalline SnO_2 for long-term isothermal annealing, Scr. Mater. 49 (2003) 441–446, https://doi.org/10.1016/S1359-6462(03)00296-3.

[69] X. Song, D. Liu, Y. Zhang, Y. Ding, M. Li, S. Wang, X. He, et al., Grain growth kinetics of SnO_2 nanocrystals synthesized by precipitation method, J. Wuhan Univ. Technol., Mater. Sci. Ed. 25 (2010) 929–934, https://doi.org/10.1007/s11595-010-0122-z.

[70] D. Bouëxière, K. Popa, O. Walter, M. Cologna, Kinetic study on the grain growth of PuO_2 nanocrystals, RSC Adv. 9 (2019) 6542–6547, https://doi.org/10.1039/C8RA10430A.

[71] P.S. Peercy, B. Morosin, Pressure and temperature dependences of the Raman-active phonons in SnO_2, Phys. Rev. B 7 (1973) 2779–2786, https://doi.org/10.1103/PhysRevB.7.2779.

[72] H. Zhu, Q. Li, C. Yang, Q. Zhang, Y. Ren, Q. Gao, N. Wang, et al., Twin crystal induced near zero thermal expansion in SnO2 nanowires, J. Am. Chem. Soc. 140 (2018) 7403–7406, https://doi.org/10.1021/jacs.8b03232.

[73] S.R. Joshi, M.A. Schroer, M. Winterer, Observing structural evolution of tin oxide nanocrystals during chemical vapor synthesis by In situ and operando X-ray diffraction, Chem. Mater. 38 (2026) 3619–3629, https://doi.org/10.1021/acs.chemmater.6c00089.